HIGH-RESOLUTION LUNAR TOPOGRAPHY FROM LASER RANGING AND PHOTOGRAPHIC DATA

Iris Fernandes, Klaus Mosegaard
Niels Bohr Institute
University of Copenhagen

ABSTRACT

Mapping landforms on the Moon is of great interest and importance for future human settlements and resources exploration. One of the first steps is to map their topography and investigate their shape and geometry in great detail and resolution, which would provide the first conditions for assessing their suitability for future on-site analysis. However, data from the Lunar Orbiter Laser Altimeter (LOLA) provide low resolution elevation maps in comparison to the size of detailed geological features. To improve resolution, we developed an inverse method to upscale topographic maps to a higher resolution constraining with photographic data from the Lunar Reconnaissance Orbiter Camera (LROC). The method, which exploits the relation between topographic gradients and degrees of shading of incoming sunlight, shows an improvement of the order of 70 times or more, bringing it to the same resolution as the optical images from LROC, and it is also potentially a way to remove shades from features such as caves. It was also possible to estimate the error of the model, considering uncertainties in the albedo. The reconstructed maps provide a remote and cheap alternative to better investigate regions of interest on planetary bodies in greater details without the aid of new and expensive engineering feats.

Keywords: planetary physics, planetary exploration, error estimation, surface mapping, computational modelling, applied geophysics, Moon surface, lunar landforms, space science

INTRODUCTION

Surveying Lunar landforms is often challenging, presenting several technical obstacles in terms of engineering, data and image processing, computational power and mathematical complexity. Interesting features are observed from the Lunar Reconnaissance Orbiter Camera (LROC) in photographic optical images in Regions of Interest (ROI) such as caves, lava tube pits, lava channels and craters under shaded areas, possibly containing water ice (Smith, D. E. et all, 1997; Smith, D. E. et all, 2010(1); Smith, D. E. et all, 2010(2)).

Mapping these areas is fundamental for any further investigation supporting the decision making in connection with future human settlements and resources exploration. For this, it is necessary to identify the surface geology, the rock composition and its spatial distribution, and similarities with Earth or other planetary bodies, to infer the possibility of accessing

ISRU (In-Situ Resource Utilization) (Johnson et all., 2010).

One of the initial stages is to map the topography and probe geological features of the landforms. All this would only be possible if the imagery data contains enough detail and resolution; poor resolution means missing important and small elements, for instance cave entrances and lava tubes.

Imagery data by NASA space craft, the Lunar Reconnaissance Orbiter Camera (LROC) provides optical photos showing images in scale of approximately half to one metre per pixels. However, the topographic data acquired by the Lunar Orbiter Laser Altimeter (LOLA) onboard LRO provides elevation maps of approximately 60 metres per pixel near the equator. This poorer resolution in comparison with the photos misses smaller surface elements, thereby increasing the uncertainty of geological interpretations.

The challenge of retrieving important small-scale features in planetary bodies has being a subject of several studies throughout the decades. In a NASA report carried by William Whittaker (2012), methodologies are discussed for developing high resolution modelling of surface and subsurface phase-I lunar mapping with sparse data, enabling robotic phase-II developments. In part of this research, a simulated area was created to imitate the view of landers or rovers - which means in higher resolution. This method shows a synthetic case where a low-resolution terrain was used and then added new small features in accordance to statistical models of Surveyor data (NASA Surveyor Project Final Report, 1968). A photo was created from this reconstructed LiDAR map. Due to the complexity of these studies it is necessary to develop elaborated robotic missions. In this same report, it is described how rovers and landers equipped with LiDAR cameras and small gadgets will be taken to lava pit entrances to investigate their interior. In this way, a series of robotic missions are made necessary to compensate for the lack of information we have from orbit in phase I.

A different approach carried by Kaku, T. et all (2017) is about mapping the lunar cave Marius Hills, whose diameter is approximately 65 metres (Haruyama, J. et al., 2009). Using SELENE Lunar Radar Sounder (LRS) they developed a technique combining LRS patterns with gravity data, showing regions with lower gravity suggesting the presence of voids, for instance, lava tubes or caves. Also, as seen in Haruyana J., et all 2012(1) and Haruyana J., et all 2012(2) SELENE data is been used to create Lunar Digital Terrain Models from terrain stereo camera observations.

Also, in an attempt to improve the resolution of small geological features, a study carried out by Barker, M.K. et al. (2015) offers improved lunar digital elevation models (DEM) presenting geo-location errors. This method uses the SELENE Terrain Camera data as constraints to remove errors in orbital pointing and positioning from topographic data from LOLA, by filling gaps in the topographic data using the TC data without the need of interpolation. Although this method is robust and presents an excellent alternative for improving DEM's, the resolution of 512 pixels per degree from LOLA data (~60m per pixel) is maintained and the resolution of the Terrain Camera photos are down-scaled to match the topographic resolution.

To help supply the need of improved remote exploration methods, we developed a new theoretical and numerical approach using an inverse problem formulation based on Tarantola and Valette (1982) and Tarantola (2005) presenting an efficient alternative to upscale the topography, constraining it with higher resolution photos from LROC. Our method uses physical properties of the area: The solar illumination angles, in combination with the photographic brightness and albedo provide information about the slopes and the direction that the terrain tends to go. Gradients can be

calculated and used to constrain the estimated high-resolution topography.

Solving the inverse problem where we have low resolution topographic maps, high resolution photos, and calculated gradients allows us to compute the high-resolution topography. The results show a significant improvement of the elevation resolution from the aforementioned 60 metres to the less than one metre (same as the photos) per pixel. To perform the inverse problems calculations, we assumed a constant albedo everywhere. The resulting uncertainties were quantified and presented along with the results.

In the theory section we derive the equations and explain in detail the theoretical approach that was developed. In the numerical methods section, we present a computational experiment in a synthetically created area to test our mathematical formulation as well as the algorithm. Finally, in the results section we apply it to real data from the Moon.

THEORETICAL FORMULATION

We base our theory on the Inverse Problems formulation presented by Tarantola and Valette's (1982) and Tarantola (2005).
Let us define the desired high-resolution topography map (matrix) $\boldsymbol{M}$, and the gradient maps $\boldsymbol{X}$ and $\boldsymbol{Y}$, providing information about the slopes from the illumination in North-South and East-West direction, respectively. The matrix $\boldsymbol{G}$ is the topography gradient operator (NS direction) and $\boldsymbol{G}'$ its transposed (the gradient operator in the EW direction).

Linear Least Squares Inversion of Image Gradient Data and Constraints from Down-sampled Data

We wish to solve the linear least squares inverse problem for the unknown high-resolution image model $\boldsymbol{M}$. Here we use the gradients derived from the photographic data as constraints:

$$\boldsymbol{GM} = \boldsymbol{X}$$
$$\boldsymbol{MG}' = \boldsymbol{Y}$$

As we want to find the high-resolution topography, we assume that the LOLA low resolution data is an up-sampled version of $\boldsymbol{M}$. To solve the problem of finding the maximum a posteriori model $\boldsymbol{M}$ (see, e.g., Tarantola (2005)), we use the LOLA low resolution topography $\boldsymbol{M}_0$ as our prior model and define the "model update" $\Delta\boldsymbol{M} = \boldsymbol{M} - \boldsymbol{M}_0$. If $\boldsymbol{X}_0$ and $\boldsymbol{Y}_0$ are rough estimates of the gradients calculated directly from the LOLA low resolution topography, we can also define "data residuals" $\Delta\boldsymbol{X} = \boldsymbol{X} - \boldsymbol{X}_0$ and $\Delta\boldsymbol{Y} = \boldsymbol{Y} - \boldsymbol{Y}_0$, and since

$$\boldsymbol{GM}_0 = \boldsymbol{X}_0$$
$$\boldsymbol{M}_0\boldsymbol{G}' = \boldsymbol{Y}_0$$

we can formulate equations for the updates:

$$\boldsymbol{G}\Delta\boldsymbol{M} = \Delta\boldsymbol{X}$$
$$\Delta\boldsymbol{M}\boldsymbol{G}' = \Delta\boldsymbol{Y}. \qquad (1)$$

Once the updates are found, we can compute the high-resolution topography estimate as

$$\boldsymbol{M} = \Delta\boldsymbol{M} + \boldsymbol{M}_0.$$

As input to these calculations, $\boldsymbol{M}_0$, $\boldsymbol{X}_0$ and $\boldsymbol{Y}_0$ are available from the LOLA data, but we need to estimate the full gradients $\boldsymbol{X}$ and $\boldsymbol{Y}$ to obtain $\Delta\boldsymbol{X}$ and $\Delta\boldsymbol{Y}$. The components of these gradients matrices are the local gradients of the topography $f(x, y)$ and they are related to the normal vector $\boldsymbol{N}(x, y)$ through:

$$\boldsymbol{N}(x,y) = \begin{pmatrix} \frac{\partial f}{\partial x}(x,y) \\ \frac{\partial f}{\partial y}(x,y) \\ -1 \end{pmatrix},$$

giving a *unit* normal vector

$$\boldsymbol{n}(x,y) = \frac{\boldsymbol{N}(x,y)}{|\boldsymbol{N}(x,y)|}.$$

If the surface at is hit by light with unit direction vector $\boldsymbol{s}$, the illumination damping factor δ is the magnitude of the projection of $\boldsymbol{s}$ on $\boldsymbol{n}(x,y)$, scaled by the albedo a:

$$\delta(x,y) = a\,\boldsymbol{s}\cdot\boldsymbol{n}(x,y)$$

giving 1 when $\boldsymbol{n}(x,y)$ and $\boldsymbol{s}$ are parallel, and 0 when $\boldsymbol{n}(x,y)$ and $\boldsymbol{s}$ are perpendicular. If we know $\boldsymbol{s}$, have an estimate of the albedo ($a \approx 0.12$ for the Moon), can get the damping factor (brightness) $\delta(x,y)$ from the photographic data, we can compute a least squares estimate of $\boldsymbol{n}(x,y)$,

$$\boldsymbol{n} = \boldsymbol{n}_0 + \boldsymbol{D}^{\boldsymbol{T}}(\boldsymbol{D}\boldsymbol{D}^{\boldsymbol{T}} + \boldsymbol{\epsilon}^{\boldsymbol{2}}\boldsymbol{I})^{-\boldsymbol{1}}(\delta - \delta_0)$$

where $\boldsymbol{D}$ is the dot product and scaling operator ($\boldsymbol{D}\boldsymbol{v} = a\,\boldsymbol{s}\cdot\boldsymbol{v}$), ϵ is a regularization parameter, $\boldsymbol{n}_0$ and δ_0 are a priori estimates of the normal vector and the brightness, respectively, computed directly from the low resolution LOLA topography. From $\boldsymbol{n}$ we can get the required gradients.

To finally solve (1) for $\Delta\boldsymbol{M}$, we need to simultaneously minimize the difference between the left-hand and the right-hand sides of these equations. That is, we need to minimize the following expression with respect to $\Delta\boldsymbol{M}$:

$$\sigma_D^{-2}\|\boldsymbol{G}\Delta\boldsymbol{M} - \Delta\boldsymbol{X}\|^2 + \sigma_D^{-2}\|\Delta\boldsymbol{M}\boldsymbol{G}' - \Delta\boldsymbol{Y}\|^2 + \sigma_M^{-2}\Delta\boldsymbol{M} \quad (2)$$

where σ_D^2 is the variance of the noise on the data, and σ_M^2 is the a priori variance of the unknown model $\boldsymbol{M}$.

It can be shown (see Appendix) that, for any matrices $\boldsymbol{A}, \boldsymbol{B}$ and $\boldsymbol{C}$ with appropriate dimensions, the derivative of the error expression:

$$E(\boldsymbol{\mathcal{M}}) = \|\boldsymbol{A}\boldsymbol{\mathcal{M}}\boldsymbol{B} - \boldsymbol{C}\|^2$$

with respect to the components of a matrix $\boldsymbol{\mathcal{M}}$ are:

$$\left\{\frac{\partial E_D}{\partial \boldsymbol{\mathcal{M}}_{pq}}\right\} = 2\boldsymbol{A}'\boldsymbol{A}\boldsymbol{\mathcal{M}}\boldsymbol{B}'\boldsymbol{B} - 2\boldsymbol{A}'\boldsymbol{C}\boldsymbol{B}\,.$$

Using this result for $\boldsymbol{\mathcal{M}} = \Delta\boldsymbol{M}$ we can now minimize expression (2) through differentiation and setting equal to zero:

$$\sigma_D^{-2}(\boldsymbol{G}'\boldsymbol{G}\Delta\boldsymbol{M} - \boldsymbol{G}'\boldsymbol{X} + \Delta\boldsymbol{M}\boldsymbol{G}'\boldsymbol{G} - \boldsymbol{Y}\boldsymbol{G}) + \sigma_M^{-2}\Delta\boldsymbol{M} = \boldsymbol{0}$$

or,

$$\sigma_D^{-2}(\boldsymbol{G}'\boldsymbol{G}\Delta\boldsymbol{M} + \Delta\boldsymbol{M}\boldsymbol{G}'\boldsymbol{G}) + \sigma_M^{-2}\Delta\boldsymbol{M} = \sigma_D^{-2}(\boldsymbol{G}'\boldsymbol{X} + \boldsymbol{Y}\boldsymbol{G})$$

This matrix equation can be rearranged to:

$$(\boldsymbol{G}'\boldsymbol{G} + \epsilon^2\boldsymbol{I})\Delta\boldsymbol{M} + \Delta\boldsymbol{M}\boldsymbol{G}'\boldsymbol{G} = \boldsymbol{G}'\boldsymbol{X} + \boldsymbol{Y}\boldsymbol{G} \quad (3)$$

Equation (2) is an equation in $\Delta\boldsymbol{M}$ of the form

$$\boldsymbol{A}\Delta\boldsymbol{M} + \Delta\boldsymbol{M}\boldsymbol{B} = \boldsymbol{C}$$

for matrices $\boldsymbol{A}, \boldsymbol{B}$ and $\boldsymbol{C}$ with appropriate dimensions. This is a so-called *Sylvester Equation* for which no closed-form solution has been found. However, a numerical solution is available. See, e.g., De Terán et al. (2016).

NUMERICAL METHOD

To demonstrate and test our method, we created a synthetic test example. This numerical experiment aims to investigate if our method and algorithm is able to reconstruct a known, controlled area. From a set of real topographic LOLA data (which in this test plays the role as the "unknown" the high-resolution map), we

computationally created a photographic image and computed, by simple downscaling, a low-resolution version of the topographic LOLA map. The synthetic photo was computed by subjecting the high-resolution topography to artificial illumination with a chosen illumination angle.

On Figure 1, we see the real LOLA topographic data from and area on the Moon located around $25{,}41\,°N$ and $2{,}83\,°E$ from SLDEM2015 Planetary Data System LOLA data node: (http://imbrium.mit.edu/EXTRAS/SLDEM2015).

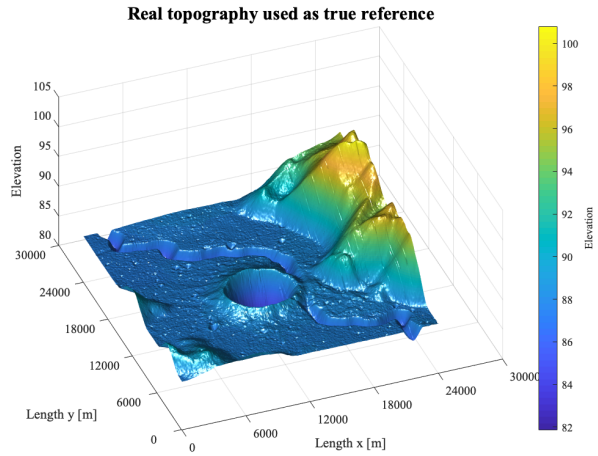

Figure 1 – Topography of the area used for the numerical example from LOLA (NASA/PDS/MIT).

From this image we used a down-sampling operator downscale it 40 times from the original one and create a low-resolution topography (Figure 2).

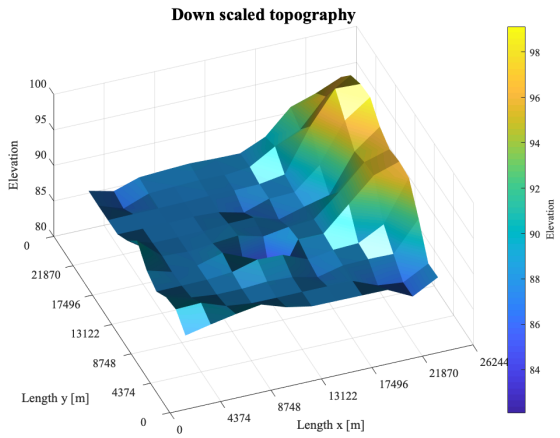

Figure 2 – Synthetic low-resolution topography, 40 times down-scaled.

To be able to perform inversion, we transformed the LOLA low resolution topographic data into a smoothed map. The resolution as shown on Figure 2 is maintained, only the number of points is increased, matching the photographic image (Figure 3). As the number of points (pixels) are different in both Figure 1 and Figure 2, we smoothed and interpolated the down-sampled topography, creating a new map with a large number of points, the same as the true reference model (Figure 3).

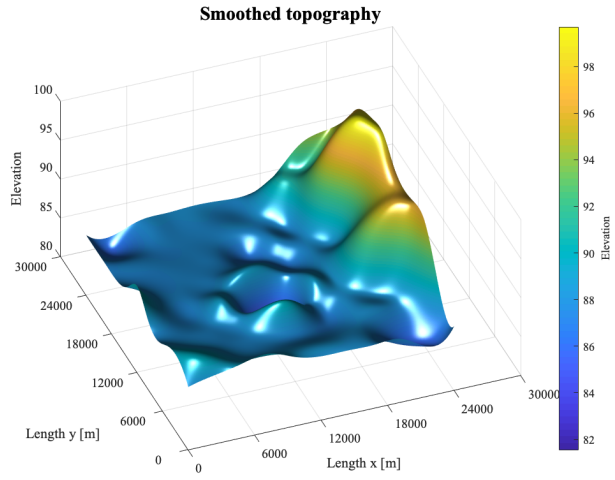

Figure 3– Smoothed low resolution topography with high number of pixels.

We created an artificial photography from Figure 1 with illumination angles: azimuth = −20° (slew angle in degrees: West = 0°, North = −90°) elevation of sun = 15° (angle of sun over horizon).

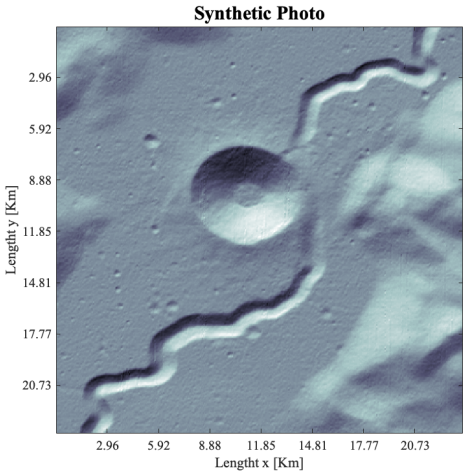

Figure 4– Synthetic optical imagery with incidence angle of 65° and azimuth of 160° degrees.

From Figure 4, both gradients in north-south and east-west directions were computed (Figure 5).

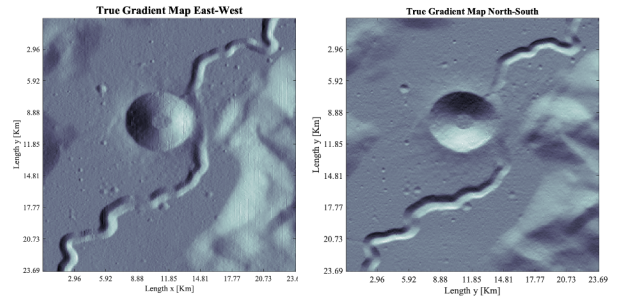

Figure 5 – Gradients of the synthetic photo image.

To provide information about the slopes, we calculated the gradients in the North-South and East-West directions from the illumination of the photographic data. Depending on the direction of the light, components of N-S or E-W will be more pertinent for the calculations; gradients from images with solar elevation angles close to zero (horizontal direction) will provide more information than close to 90° (vertical), and vice-versa.

It is important to notice here that we have two different angles.
As shown on Figure 6 scheme, the influence of the gradients will be 74% for the north-south direction and 26% for the east-west direction. It is possible to see the shadow coming from the Sub Solar Azimuth angle (Figure 6a). The incidence angle represents the angle in relation to the surface (Figure 6b).

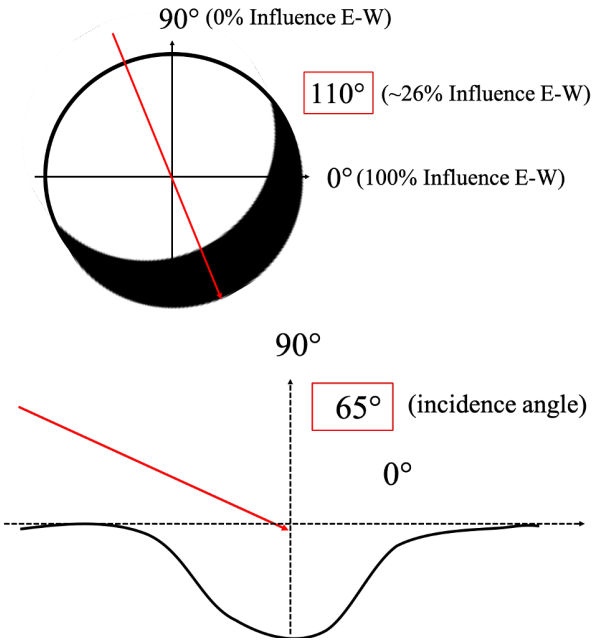

Figure 6 – Influence of the gradients (slopes) depending on the incidence angle. A) Top figure shows the illumination and shadow from the azimuth angle. B) Bottom figure shows the incidence angle.

Performing the least-squares inversion, we computed the high-resolution topography using the down-sampled low-resolution topography and the synthetic photo as constrains and the result can be seen on Figure 7.

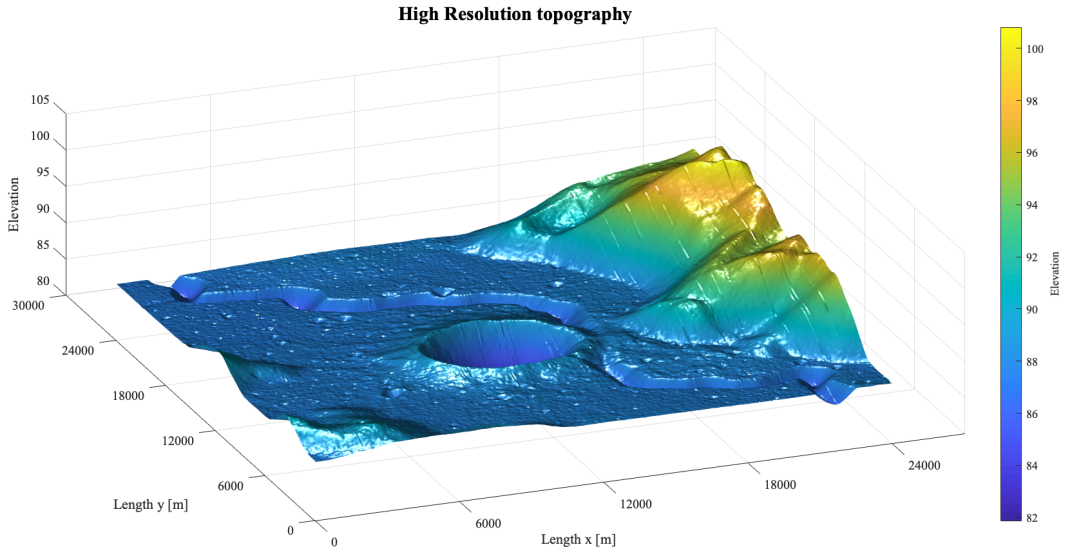

Figure 7 – Computed synthetic high-resolution topography.

To verify the precision, Figure 8 shows a cross-section of the initial high-resolution reference (Figure 1) with the computed from the inversion (Figure 6*)*.

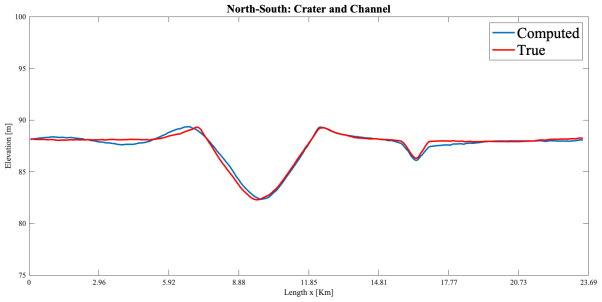

Figure 8 – Cross-section of the initial and computed terrain maps.

It is observed that the computed topography is very close the to the initial test example. From the low-resolution elevation map, it was not possible to observe the finer details seen on the photo image. These details were retrieved after inversion is performed, as shown in the high-resolution elevation map.

RESULTS

We use now the real imagery data of an area centred around $22{,}23\,^{\circ}N$ and $29{,}61\,^{\circ}E$, in the Region of Interest (ROI) of the Apollo 15 landing site. The area ranges approximately $5881m \times 5881m$.

The optical image data covering this area was provided by LROC, observations M1249338893R, M1249338893L, M1249345927R, M1249345927L, combined by Klem, S. et all (2014) (Figure 9) with a resolution of 0,9 m per pixel.

On Figure 9, the lava channels, craters and other surface features are shown illuminated with sun light with an incidence angle of $65{,}88\,^{\circ}$ and an azimuth angle of $81{,}76\,^{\circ}$.

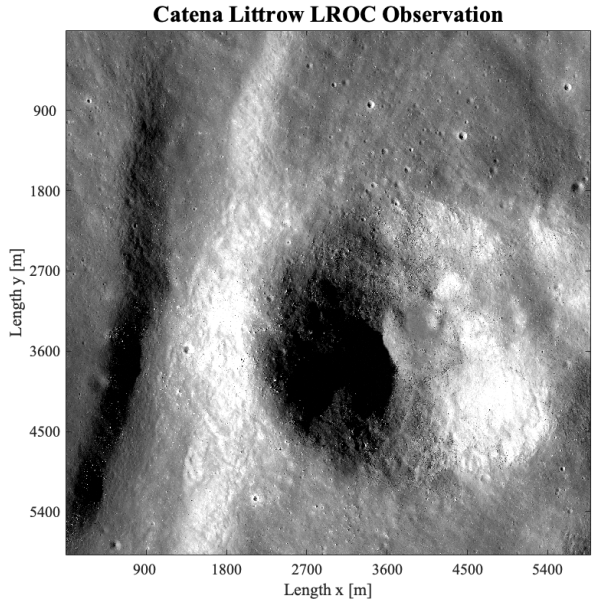

Figure 9 – Lunar landforms with illumination and incidence angle of 65,88° from LROC (NASA/GSFC/Arizona State University).

The topographic map of the area can be seen on Figure 10. Acquired by *LOLA, 2015,* the resolution is 512 pixels per degree, corresponding to $59{,}225m$ per pixel.

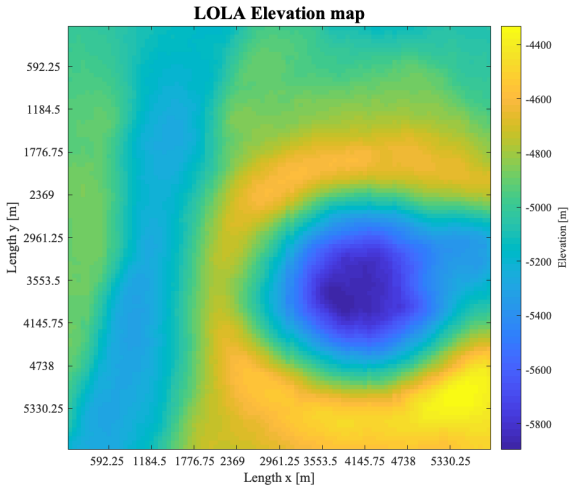

Figure 10 – Topography of the area covering the Catena Littrow ROI from LOLA (NASA/PDS/MIT).

We calculated the gradients of the photo showing the influence of light on the surface structures. The influence of light is 47% in the East-West direction and 53% in the North-South direction.

To be able to perform inversion, a smoothed version of the low-resolution LOLA data (Figure 10) was computed, generating a same resolution image but with a larger number of points.

Small scaled features are revealed on Figure 11b. Craters to the size up to ~25 metres can be observed from the reconstructed up-scale elevation map.

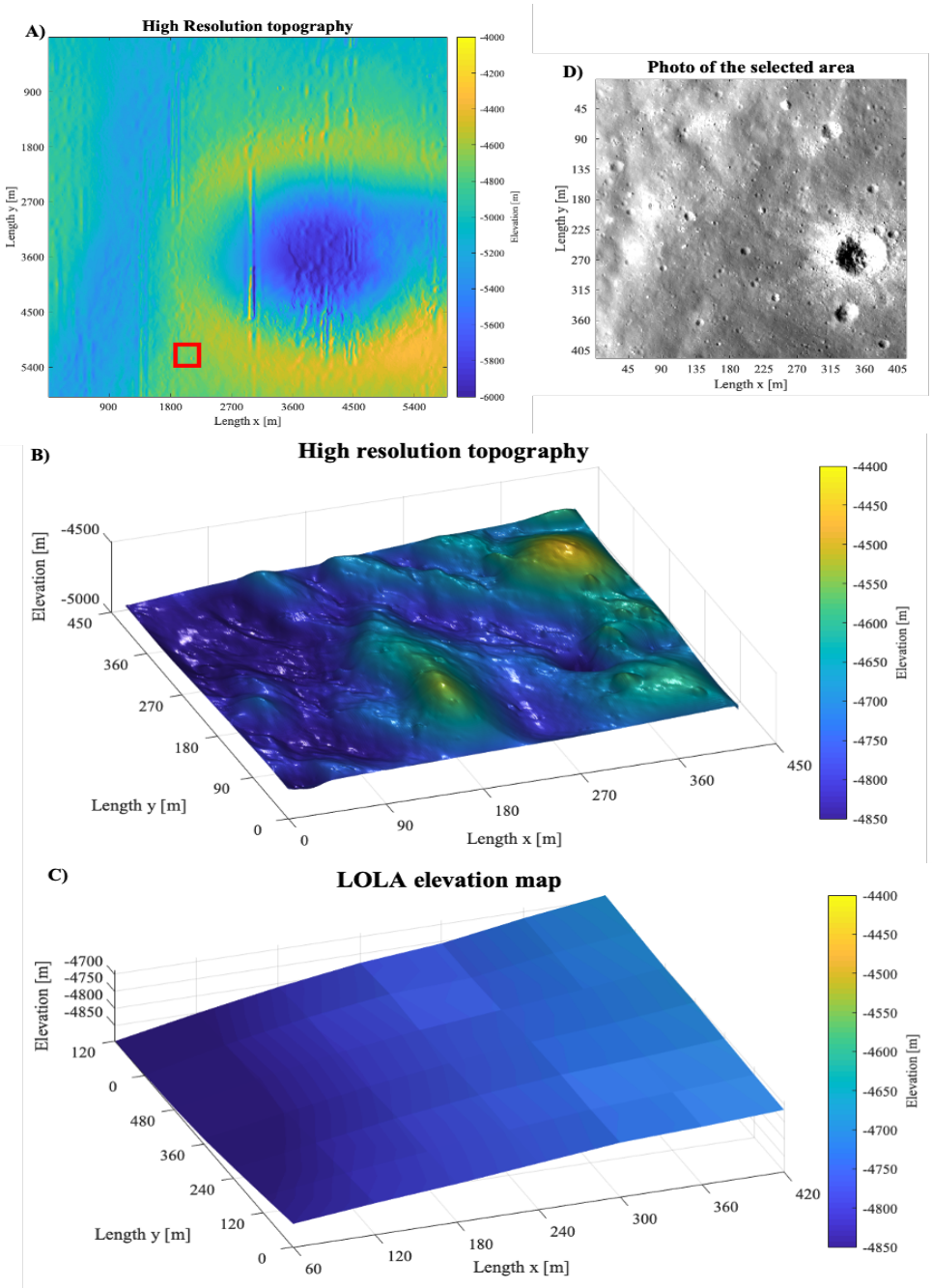

Figure 11 – A) Computed high-resolution topographic map. B) High-resolution section area. C) LOLA elevation data. D) LROC observation of the section area.

In the detailed area shown on Figure 11, we verify a cross-section comparing the initial LOLA data, the smoothed up scaled low resolution and our computed high-resolution elevations (Figure 12).

The high-resolution cross-section (Figure 12c) shows the elevations of small craters, completely unseen from the initial LOLA resolution (Figure 12b). Also, in the smoothed section (Figure 12b), it is possible to observe that the elevation is averaged, and the terrain features are not clearly represented.

The precision of positions in the elevation are influenced by numerical assumptions we had to made. We assumed constant albedo everywhere, so all the variation in the illumination of the surface is assumed to be from the slopes. This will add uncertainties in positions of the elevation map.

Assuming a Gaussian uncertainty on the albedo with a standard deviation of 20%, we estimated the spatial distribution of the uncertainties in elevation. Figure 13 shows an uncertainty map of the topography.

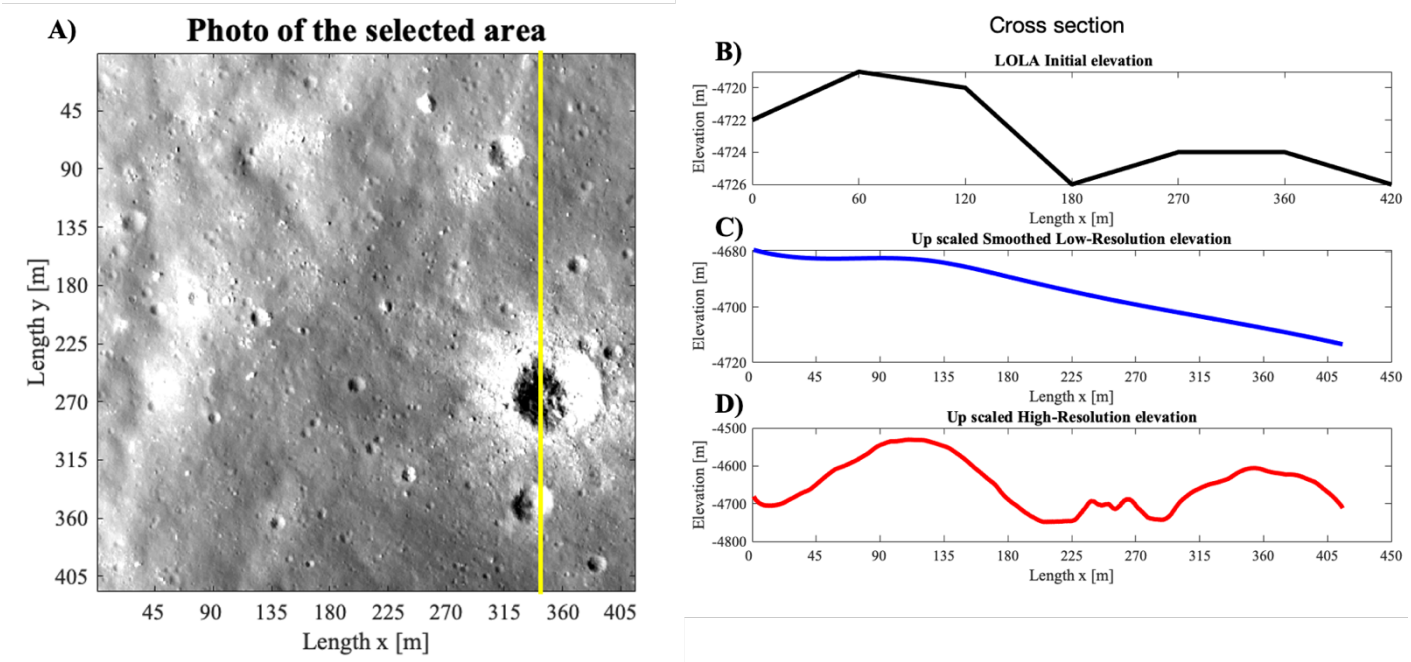

Figure 12 – A) Cross section of the area. B) Elevation data from LOLA. C) Smoothed up scaled elevation. D) Computed high-resolution elevation.

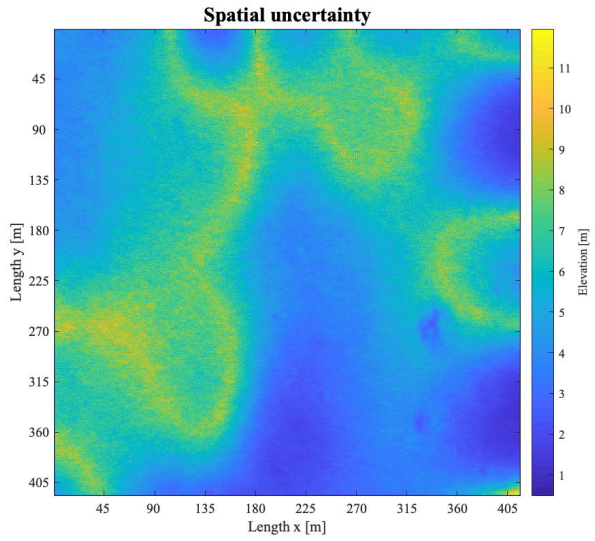

Figure 13 – Spatial uncertainty map of the elevation.

It is possible to see that the uncertainties range from $0.5\,m.$ to ~12 m and are, as expected, higher where the illumination is near-perpendicular to the terrain.

DISCUSSION

We tested our method in a numerically produced dataset based on real data from LOLA. The low-resolution topography was a down-sampled case of the real data and a synthetic optical image was generated by artificial lightening with a given illumination angle applied to the original LOLA topography.

Real data was then considered, and we computed an upscaled topography. The inverse problem formulation used illumination angles and brightness, assuming constant albedo. The spatial distribution of the uncertainty was then computed.

In the high resolution elevation maps from Figure 7 and Figure 11a, we can observe N-S stripes that go across the area. This is from errors in the data acquisition that creates offsets in these LOLA profiles (Barker, M.K. et al. (2015)). During the inversion, they are amplified as the method interprets them as terrain features. They are not seen in, or influencing the small section area (Figure 11b), though.

As we consider constant albedo, small features close to the crater rims might be amplified and seen as small elevations. The uncertainty map on Figure 13, shows higher uncertainty around one of the craters. Adjustable parameters can be modified to minimize this effect. Although this is a limitation of the method, this only starts to appear in geological features of approximately 25 metres diameter and show a maximum uncertainty in elevation of 12 metres.

In the initial resolution provided by LOLA data, it is only possible to observe large geological features in the scale of hundreds of metres, as one pixel has ~60 metres. Our up-scaled and high-resolution results offer a way to detect structures in the size of small craters and lava pit entrances that are under shades. The method, therefore, is an alternative to remove shades from these structures and examine their interior.

CONCLUSION

In this study, we developed a computational method that uses topographic data from the Lunar Orbiter Laser Altimeter (LOLA) onboard the Lunar Reconnaissance Orbiter (LRO) constrained by optical images from LRO camera (LROC) in order to create an upscaled Digital Elevation Model (DEM) of lunar landforms.

The topographic data resolution is 512 pixels per degree, which provides a ~60 metres per pixel resolution. Constraining our inverse problem formulation with photos with resolution of 0,9 metres per pixel, we were able to compute a final topographic map upscaled to the same photo resolution.

In our formulation, we assumed constant albedo, therefore, the brightness is assumed to be exclusive from the slopes. For this reason, we also computed the spatial uncertainty which was in the order of 0.50 metres to 11.96 metres.

The results provide a high-resolution and upscaled DEM, being able to map geological structures of the scale of around 25 metres. Hence, our formulation provides not only a high resolution imagery but also a new technique to remove shades from features such as caves or lava pit entrances. This method also offers an alternative to study in greater details regions of interest without the need of expensive engineering feats.

Future perspectives of this work are to improve the capabilities of this method to map formations of more sophisticated and challenging shapes and smaller-scaled sizes, as well as considering different physical properties available.

APPENDIX

Minimization of a General Misfit

Consider minimization of the general expression with respect to the matrix $\boldsymbol{\mathcal{M}}$:

$$E_D(\boldsymbol{\mathcal{M}}) = \|\boldsymbol{G\mathcal{M}F'} - \boldsymbol{D}\|^2 = \sum_i \sum_j \left[D_{ij} - \sum_k \sum_l G_{ik}\mathcal{M}_{kl}F_{jl} \right] \left[D_{ij} - \sum_m \sum_n G_{im}\mathcal{M}_{mn}F_{jn} \right]$$

where G, F and D are matrices. Multiplying the square brackets and reversing the order of the summations gives

$$E_D(\boldsymbol{\mathcal{M}}) = \sum_k \sum_l \sum_m \sum_n \mathcal{M}_{kl}\,\mathcal{M}_{mn} \sum_i \sum_j G_{ik}F_{jl}G_{im}F_{jn} - 2\sum_m \sum_n \mathcal{M}_{mn} \sum_i \sum_j D_{ij}G_{im}F_{jn} + \sum_i \sum_j D_{ij}D_{ij}$$

We can now compute the derivatives $\partial E_D / \partial \mathcal{M}_{pq}$ term by term:

$$\frac{\partial}{\partial M_{pq}} \sum_k \sum_l \sum_m \sum_n \mathcal{M}_{kl}\,\mathcal{M}_{mn} \sum_i \sum_j G_{ik}F_{jl}G_{im}F_{jn} = \sum_k \sum_l \sum_m \sum_n \left[\delta_{(kl)(pq)}\mathcal{M}_{mn} + \mathcal{M}_{kl}\delta_{(mn)(pq)} \right] \sum_i \sum_j G_{ik}F_{jl}G_{im}F_{jn}$$

$$= \sum_k \sum_l \left(\delta_{(kl)(pq)} \sum_m \sum_n \mathcal{M}_{mn} \sum_i \sum_j G_{ik}F_{jl}G_{im}F_{jn} + \mathcal{M}_{kl} \sum_m \sum_n \delta_{(mn)(pq)} \sum_i \sum_j G_{ik}F_{jl}G_{im}F_{jn} \right)$$

$$= 2\sum_m \sum_n \mathcal{M}_{mn} \sum_i \sum_j G_{ip}F_{jq}G_{im}F_{jn}$$

and

$$\frac{\partial}{\partial M_{pq}}\left(-2\sum_m\sum_n \mathcal{M}_{mn}\sum_i\sum_j D_{ij}G_{im}F_{jn}\right)$$

$$= -2\sum_m\sum_n \delta_{(mn)(pq)}\sum_i\sum_j D_{ij}G_{im}F_{jn}$$

$$= -2\sum_i\sum_j D_{ij}G_{ip}F_{jq}$$

and

$$\frac{\partial}{\partial \mathcal{M}_{pq}}\left(\sum_i\sum_j D_{ij}D_{ij}\right) = 0.$$

All in all, we have:

$$\frac{\partial E_D}{\partial \mathcal{M}_{pq}} = 2\sum_m\sum_n \mathcal{M}_{mn}\sum_i\sum_j G_{ip}F_{jq}G_{im}F_{jn} - 2\sum_i\sum_j D_{ij}G_{ip}F_{jq}$$

$$= 2\sum_m\sum_n\sum_i\sum_j G_{ip}G_{im}\mathcal{M}_{mn}F_{jn}F_{jq} - 2\sum_i\sum_j G_{ip}D_{ij}F_{jq}$$

$$= 2\sum_m\sum_n\sum_i\sum_j G'_{pi}G_{im}\mathcal{M}_{mn}F'_{nj}F_{jq} - 2\sum_i\sum_j G'_{pi}D_{ij}F_{jq}$$

or, in matrix notation,

$$\left\{\frac{\partial E_D}{\partial \mathcal{M}_{pq}}\right\} = 2\boldsymbol{G'GMF'F} - 2\boldsymbol{G'DF} \qquad (3)$$

REFERENCES

Barker, M.K., E. Mazarico, G.A. Neumann, M.T. Zuber, J. Haruyama, and D.E. Smith. "A New Lunar Digital Elevation Model from the Lunar Orbiter Laser Altimeter and SELENE Terrain Camera." Icarus 273 (July 2016): 346–355.

De Terán, F., Iannazzo, B., Poloni, F., Robol, L., 2017, Solvability and uniqueness criteria for generalized Sylvester-type equations. ArXiv.org: 10.1016/j.laa.2017.10.018

Haruyama, J. et al., 2009. Possible lunar lava tube skylight observed by SELENE cameras. In: Advancing Space and Earth Sciences (AGU), Vol.36, Issue 21. DOI: doi.org/10.1029/2009GL040635

Haruyama, J. et al., 2012. Lunar global digital terrain model dataset produced from SELENE (Kaguya) terrain camera stereo observations. In: Lunar and Planetary Science Conference, p. 1200.

Haruyama, J. et al., 2014. Data products of SELENE (Kaguya) Terrain Camera for future lunar missions. In: Lunar and Planetary Science Conference, p. 1304.

Johnson, A., et al., 2010. An integrated traverse planner and analysis tool for plane- tary exploration. Am. Inst. Aeronaut. Astronaut. doi:10.2514/6.2010-8829, http: //dx.doi.org/10.2514/6.2010- 8829.

Kaku, T., Haruyama, J., Miyake, W., Kumamoto, A., Ishiyama, K., Nishibori, T., ... Howell, K. C. (2017). Detection of intact lava tubes at Marius Hills on the Moon by SELENE (Kaguya) lunar radar sounder. Geophysical Research Letters, 44, 10,155–10,161. https://doi.org/ 10.1002/2017GL074998

Klem, S. M., Henriksen, M. R., Stopar, J., Boyd, A., & Robinson, M. S. (2014). Controlled LROC Narrow Angle Camera High Resolution Mosaics. In *Lunar and Planetary Science Conference* (Vol. 45, abstract #2885).

Mosegaard, K., and Hansen, T. M., 2016. Inverse Methods: Problem formulation and Probabilistic Solution. Chapter 2, Integrated Imaging of the Earth, Theory and Applications. AGU, ISBN: 978-1-118-92905-6.

Mosegaard, K., and Tarantola, A., 1995. Monte Carlo sampling of solutions to inverse problems: Journal of Geophysical Research 100, B7, pp. 12431-12447.

NASA Surveyor Project Final Report. NASA Jet Propulsion Laboratory. (1968).

SLDEM2015 Planetary Data System LOLA data node:(http://imbrium.mit.edu/EXTRAS/ SLDEM2015).

Smith, D.E., et al., 1997. Topography of the Moon from the Clementine LIDAR. J. Geo- phys. Res. 102, 1591. doi:10.1029/96JE02940.

Smith, D.E., et al., 2010. Initial observations from the Lunar Orbiter Laser Altimeter (LOLA). Geophys. Res. Lett. 37, 18204. doi:10.1029/2010GL043751.

Smith, D.E., et al., 2010. The Lunar Orbiter Laser Altimeter investigation on the Lu- nar Reconnaissance Orbiter Mission. Space Sci. Rev. 150, 209–241. doi:10.1007/ s11214- 009-9512- y.

Tarantola, A., and B. Valette, 1982, Inverse problems = quest for information: Journal of Geophysics Research, 50, 150-170.

Tarantola, A., Inverse Problem Theory and Methods for Model Parameter Estimation. Siam, Philadelphia, 2005.

William Whittaker (2012), Technologies Enabling Exploration of Skylights, Lava Tubes and Caves, NASA Innovative Advanced Concepts (NIAC) Phase I.